Yamada and Kanemitsu *NPG Asia Materials* (2022) 14:48
https://doi.org/10.1038/s41427-022-00394-4

NPG Asia Materials

REVIEW ARTICLE Open Access

Electron-phonon interactions in halide perovskites

Yasuhiro Yamada[1] and Yoshihiko Kanemitsu[2]

Abstract

Strong electron-phonon interactions are frequently considered the origin of the unique electrical and optical properties of lead halide perovskites. Electron-phonon interactions induce the formation of a polaron, which is a charge carrier dressed with a phonon cloud. The details of polaron formation are crucial for carrier transport since polaron formation leads to a larger effective mass of a carrier. Several mechanisms have been proposed regarding the physics of polaron formation in halide perovskites, but the details are still under active debate. While the Fröhlich interaction plays an essential role in ionic crystals, we also need to consider the strong phonon anharmonicity of halide perovskites that may lead to the formation of an unconventional polaron. In this review article, we discuss the uniqueness of perovskite semiconductors from the viewpoint of electron-phonon interactions. We review the experimental results and the proposed models concerning the effective carrier mass and carrier mobility. Finally, we briefly explain two physical phenomena related to strong electron-phonon interactions: strong anti-Stokes photoluminescence and slow hot-carrier cooling.

Introduction

During the last decade, metal halide perovskites have attracted much attention as promising materials for solar cells and light-emitting devices[1,2]. Extensive research to date has revealed that the high performance of perovskite-based devices is mainly the result of their excellent optical properties, such as high luminescence efficiencies and long carrier lifetimes[3–6]. Furthermore, unique thermoelectric properties[7] and nonlinear optical properties have also been reported in halide perovskites[8–10], enhancing the broad interest in this class of materials. From a practical point of view, it is attractive that elemental substitution can significantly change the physical properties; that is. by substituting halogen atoms (I, Br, and Cl), the bandgap energy can be tuned over the whole visible range[11]. Additionally, high-quality halide perovskite single crystals, thin films, and nanostructures can be easily fabricated by a solution process. It is also significant to mention the small Young's moduli of these perovskites compared with those of conventional inorganic semiconductors[12], which are promising for flexible device applications[13].

Strong electron-phonon interactions have frequently been discussed regarding their roles in the physical mechanism determining the unique features of halide perovskites that distinguish them from conventional semiconductors. In particular, electron-phonon interactions lead to the formation of a polaron state, where an electron or a hole deforms the lattice in its vicinity and becomes more localized[14]. Polaron formation is accompanied by an increase in the effective carrier mass and significantly impacts the electrical and optical properties. To date, the conventional Fröhlich interaction originating from the ionic nature of perovskite crystals has been mainly considered to be the polaron formation mechanism in halide perovskites[15–17]. However, there have been several suggestions regarding the possibility that the formation of unconventional polarons is induced by the unique properties of halide perovskites, such as their soft lattice nature, a permanent dipole of the A-site cation, or a liquid-like Debye relaxation mode at low frequencies[18–24].

Polaron formation leads to a range of intriguing effects but is often detrimental for device applications. The most significant impact appears in the carrier transport properties; specifically, the reported carrier mobilities of halide

Correspondence: Yasuhiro Yamada (yasuyamada@chiba-u.jp) or Yoshihiko Kanemitsu (kanemitu@scl.kyoto-u.ac.jp)
[1]Graduate School of Science, Chiba University, Inage, Chiba 263-8522, Japan
[2]Institute for Chemical Research, Kyoto University, Uji, Kyoto 611-0011, Japan

perovskites are relatively lower than those in conventional inorganic semiconductors, which has been considered to be due to the polaron effect[16,18]. Moreover, strong electron-phonon interactions can significantly modify the band-edge optical spectra[25] and induce a slow relaxation of hot carriers[26–28]. It has also been pointed out that the formation of small polarons is deeply related to the photodegradation/self-healing mechanism as a problem in the actual use of devices[23,29–31]. Consequently, clarifying the polaron formation mechanism and its influence on the material characteristics is crucial for fundamental materials science and device applications.

In this review article, we focus on fundamental experimental research regarding the electron-phonon interactions in halide perovskites. In particular, we introduce the research performed thus far on the effective carrier mass and carrier mobility. We combine these results with a discussion to improve the understanding of the present issues in research regarding the polaron formation mechanism in halide perovskites. In addition, we show the unique physical phenomena that originate from electron-phonon interactions and mention the possibility of utilizing them in devices.

Fundamental properties of halide perovskites

Before we discuss the electron-phonon interactions in halide perovskites, we provide an overview of the characteristics of this materials system in this section. The ABX_3 perovskite structure is composed of a three-dimensional network of BX_6 octahedra, as shown in Fig. 1. With respect to the three components A, B, and X, the following atoms and molecules are commonly used: A = Cs, CH_3NH_3, $CH(NH_2)_2$; B = Pb, Sn; and X = I, Br, and Cl. Hereafter, CH_3NH_3 and $CH(NH_2)_2$ are referred to as methylammonium (MA) and formamidinium (FA), respectively. The stability of a perovskite structure can be characterized by the tolerance factor ($t = \frac{r_A + r_X}{\sqrt{2}(r_B + r_X)}$). Here, r_A, r_B, and r_X are the radii of the A-, B-, and X-site ions, respectively. It is empirically known that a perovskite crystal is stable in the range $0.8 < t < 1$. Note that the room-temperature crystal structure tends to exhibit a lower symmetry as t decreases according to the sequence of the crystal structure cubic → tetragonal → orthorhombic[32]. Similarly, halide perovskites undergo phase transitions in the sequence cubic → tetragonal → orthorhombic as the temperature decreases[33–35].

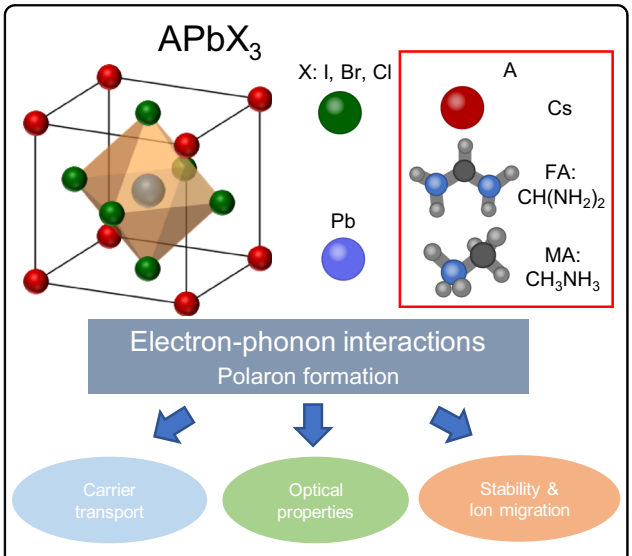

Fig. 1 Unique features of lead halide perovskites related with electron-phonon interactions. Crystal structure of $APbX_3$ lead halide perovskites and overview of important physical properties affected by electron-phonon interactions.

To bring the tolerance factor into the region where a lead perovskite structure is stable, it is necessary to employ a large-sized ion such as molecular MA^+, FA^+, or a monoatomic Cs^+ as the A-site cation (see Fig. 1b) because lead has a large ion radius. MA^+ and FA^+ ions possess a permanent dipole, which gives rise to Debye relaxation in the GHz frequency region due to its orientation relaxation in the cubic phase[20]. This orientation motion is frozen out in the low-temperature tetragonal and orthorhombic phases. Interestingly, such a relaxation mode has also been observed in Cs-based perovskites, attributable to the hopping motion of an off-centered Cs ion between the equivalent potential minima[18,36].

The phonon structure of halide perovskites has been investigated in detail using Raman scattering, neutron scattering, and terahertz (THz) spectroscopy[37–41]. We briefly mention the experimental results obtained by THz time-domain spectroscopy, where the characteristic changes in the phase and intensity of a reflected THz pulse allow us to determine the complex dielectric constant (ε) of a material. The obtained complex reflectivity spectra in the THz region contain features corresponding to different lattice vibration modes of the crystal. Figure 2 displays the spectra of the imaginary part of the dielectric constant for $MAPbX_3$ (X = I, Br, and Cl) at approximately 10 K. The phonon modes originating from the PbX_6 cage and the MA cation can be identified; that is, the black closed circles correspond to the cage modes, and the arrows correspond to the MA cation modes. At low temperatures, the optical phonons related to the PbX_6 cage are split due to the symmetry reduction caused by the phase transition. In Fig. 3a–c, we show the energy loss function $\mathrm{Im}(-1/\varepsilon)$ spectra of the cage modes for $MAPbI_3$, $MAPbBr_3$, and $MAPbCl_3$, respectively. The peak positions correspond to the longitudinal optical (LO) phonon energies. While there is no splitting of the LO phonon mode at higher temperatures (a single peak is confirmed in the cubic and tetragonal phases), a clear mode splitting appears in the orthorhombic phase. As shown in Fig. 3d, e, the optical phonon mode splits into two peaks (filled circles)

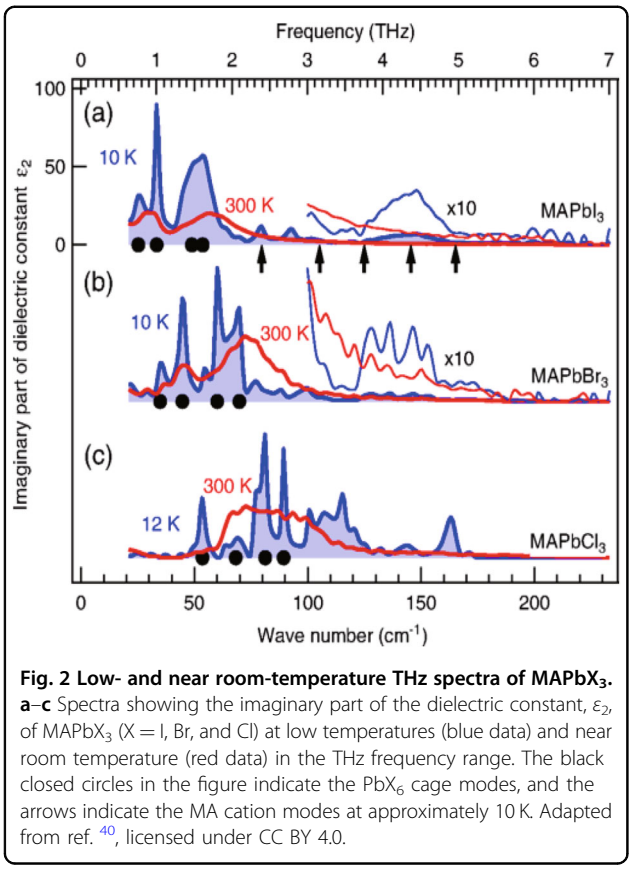

Fig. 2 Low- and near room-temperature THz spectra of $MAPbX_3$. **a**–**c** Spectra showing the imaginary part of the dielectric constant, ε_2, of $MAPbX_3$ (X = I, Br, and Cl) at low temperatures (blue data) and near room temperature (red data) in the THz frequency range. The black closed circles in the figure indicate the PbX_6 cage modes, and the arrows indicate the MA cation modes at approximately 10 K. Adapted from ref. [40], licensed under CC BY 4.0.

in the orthorhombic phase, but the weighted average of the phonon energies (open squares) remains almost unchanged.

One of the outstanding phonon characteristics of halide perovskites is their low optical phonon frequencies, attributable to the heavy lead ions. Furthermore, the linewidth of the phonon absorption is very broad at room temperature, indicating that the optical phonons are overdamped[40,41]. Phonon overdamping is considered to be due to the large phonon anharmonicity caused by the soft lattice nature of halide perovskites. Such large phonon anharmonicity might greatly influence the physical properties, especially electron-phonon interactions, and is one factor that makes a large difference between conventional semiconductors and halide perovskites.

The role of electron-phonon interactions in polaron formation

A polaron is a quasiparticle formed by an electron (or a hole) accompanying a polarization field. The carrier becomes localized and moves more slowly by covering itself with a phonon cloud. Polarons are categorized into large and small polarons according to the degree of the spatial localization of the carrier. In a large polaron, the carrier is spatially spread over more than a few lattice sites. The prototypical model of the large polaron was proposed by H. Fröhlich[42]. Note that a large polaron is formed by long-range interactions and is characterized by coherent transport. Conversely, a small polaron is localized within a single site and is usually formed by short-range electron-phonon interactions. Due to the strong localization, the electrical conduction of small polarons is dominated by the hopping process, which generally results in quite low mobility (« 1 cm^2/Vs)[14].

Long-range interactions

The Fröhlich model addresses the electrons in ionic crystals or polar semiconductors and considers the long-range interaction between an electron and a polar optical phonon mode under the continuum approximation. In this model, the strength of the electron-phonon interaction is characterized by the Fröhlich coupling constant α_e, as defined below:[14,43,44]

$$\alpha_e = \left(\varepsilon_\infty^{-1} - \varepsilon_0^{-1}\right)\sqrt{m_e^b e^4/2\hbar^3\omega_{\mathrm{LO}}}. \quad (1)$$

Here, ε_∞ and ε_0 are the high-frequency and low-frequency limits of the dielectric constant, respectively, m_e^b is the effective mass of the electron in the case of no electron-phonon interaction (bare band mass), and ω_{LO} describes the LO phonon frequency. The coupling constant between a hole and a phonon, α_h, can be simply obtained by replacing m_e^b with the effective mass of the hole in the case of no electron-phonon interaction, m_h^b.

In the case that α_e is small, the polaron relaxation energy is approximately given by $\alpha_e\hbar\omega_{LO}$, and $m_e^{pol}/m_e^b = 1 + \alpha_e/6 + 0.0236\alpha_e^2$, where m_e^{pol} is the polaron mass[14,43,44]. In addition, the polaron radius can be expressed in terms of m_e^b and ω_{LO}; $r_p^e = \sqrt{\frac{\hbar}{2m_e^b\omega_{\mathrm{LO}}}}$.

In conventional ionic inorganic semiconductors, the Fröhlich coupling constant is significantly smaller than unity[43]. On the other hand, much higher values of approximately 1 to 3 have been reported for the Fröhlich coupling constants of halide perovskites[18,45], which are rather close to those of insulators such as alkali halides and $SrTiO_3$[43].

Regarding halide perovskites, the possibility that an A-site cation with a permanent dipole leads to the formation of an unconventional large polaron has been considered extensively. The orientational motion of A-site cations, such as FA^+ and MA^+, forms a Debye relaxation mode in the GHz frequency region in the cubic phase. Miyata and Zhu proposed a model where such a dipole induces a ferroelectric local order via its Coulomb interaction with carriers, thereby creating an unconventional polaron (a ferroelectric large polaron)[18,20].

Short-range interactions

Even in the case of a covalent crystal, where a Fröhlich interaction does not occur, polaron formation is possible

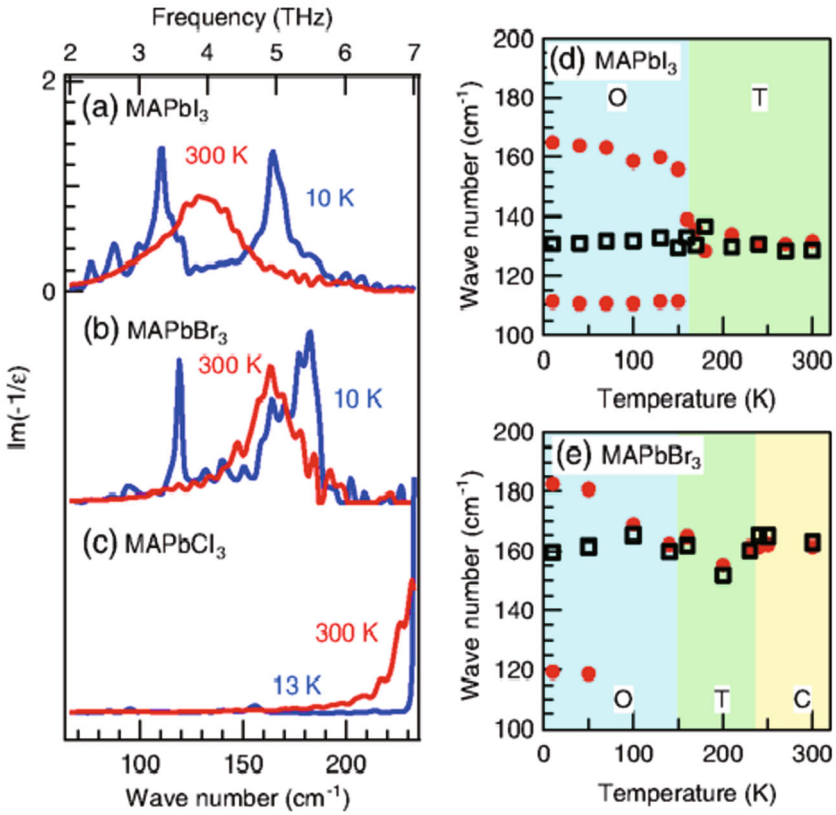

Fig. 3 Temperature dependent LO phonon energies of $MAPbX_3$. a–c Im(−1/ε)-spectra of $MAPbX_3$ (X = I, Br, and Cl) at low temperatures (10 and 13 K) and at 300 K. The peaks show the LO phonon modes originating from the PbX_6 cage. **d**, **e** The red data points show the temperature dependences of the LO phonon energy for $MAPbI_3$ and $MAPbBr_3$, respectively. The open squares show the weighted average of the phonon wavenumber. Adapted from ref. [40], licensed under CC BY 4.0.

because of short-range electron-phonon interactions. Due to the lattice deformation produced by an electron in its vicinity, a local change in the band structure occurs (deformation potential), localizing the charge carriers. Usually, a polaron caused by such a short-range interaction is strongly localized (in other words, a small polaron is formed). In the case of Fröhlich polarons, the degree of localization changes continuously according to the Fröhlich coupling constant. However, in the case of short-range interactions, a phase transition from a free-carrier state to a self-trapped state occurs if the electron-phonon interaction strength is above a specific threshold value[46,47]. It is known that the polaron mass in several alkali halides is several orders larger than the bare mass due to such a small-polaron formation, and thus the carriers are essentially immobile (typical carrier mobility in such cases is $\mu \ll 1$ cm^2/Vs)[14,47]. Although the room-temperature carrier mobility of lead halide perovskites is not as small as that of small polarons, theoretical approaches such as density functional theory (DFT) simulations have suggested possible small-polaron formation in $MAPbI_3$ due to volumetric strain and reorientation of MA cations[48]. It has been discussed that small polarons are the origin of light-induced degradation via large structural deformations generated by strongly localized carriers[23,30,31]. Moreover, an unconventional short-range interaction has been proposed as a possible carrier localization mechanism, a temporally and spatially fluctuating potential caused by a dynamical disorder resulting from the orientational motion of A-site cations or the soft nature of the lattice[19,21,24].

As a metric for the strength of short-range electron-phonon interactions that can be estimated experimentally, we can consider the steepness parameter σ_0, which is defined by the following equation of the temperature dependence of the Urbach energy:[49–51]

$$E_U(T) = \frac{\hbar\omega_{ph}}{2\sigma_0}\left(\coth\left(\frac{\hbar\omega_{ph}}{2k_BT}\right) + X\right) \quad (2)$$

where $\hbar\omega_{ph}$ is the energy of the phonon involved with the tail absorption process and X represents the contribution

of extrinsic factors such as defects or lattice strain to the absorption tail. The Urbach energy $E_U(T)$ is a parameter that characterizes the low-energy tail of the absorption spectrum $\alpha(E)$ and is defined by

$$\alpha(E) = \alpha_0 \exp\left(\frac{E - E_0}{E_U}\right), \quad (3)$$

where E_0 is the Urbach focus energy. At high temperatures ($k_B T \gg \hbar\omega_{ph}$), the Urbach energy is approximated as $E_U(T) = \frac{k_B T}{\sigma_0}$, which enables us to estimate the steepness parameter experimentally.

According to the theory of Toyozawa et al., the steepness parameter can be written as $\sigma_0 = s\frac{B}{E_R}$, where s is a dimensionless parameter that is determined only by the geometrical structure of the lattice, B is the band width, and E_R is the lattice relaxation energy[46,47]. Consequently, σ_0 is reduced for stronger electron-phonon interactions. It has been theoretically predicted that a self-trapped exciton becomes more stable than a free exciton when the steepness parameter is below a critical value (in the case of a simple cubic structure, this value is $\sigma_c^d = 1.64$ for direct transitions and $\sigma_c^{ind} = 0.93$ for indirect transitions). This relation has been confirmed in many materials[46,47]. The steepness parameters of halide perovskites exceed this critical value to some degree (σ_0 lies in the range 1.7~2.5)[52–55], suggesting that self-trapped excitons are not formed. As it is also clear that there is no long-range Coulomb interaction between a polar optical phonon and an exciton, which is an electrically neutral elementary excitation, the steepness parameter is related to short-range electron-phonon interactions.

Electron-phonon coupling in halide perovskites

Based on the above discussion, we now consider the peculiarity of perovskites from the viewpoint of electron-phonon interactions. To provide an overview, we show the inverse of the steepness parameter σ_0 as a function of the Fröhlich coupling constant α_e for various materials in Fig. 4. Here, we can consider that α_e and $1/\sigma_0$ correspond to the strength of the long- and short-range electron-phonon interactions, respectively. Note that σ_0 is extracted from the experimental results at high temperatures where $k_B T \gg \hbar\omega_{ph}$ is fulfilled. Notably, in contrast to σ_0, α_e is the ideal value derived in the framework of Fröhlich theory using parameters such as the dielectric constant, the LO phonon energy, and the bare electron mass. Except for halide perovskites, a positive relation between α_e and $1/\sigma_0$ can be seen for many materials (the blue data points in Fig. 4). These materials are confirmed to lie on the same trend line. In other words, materials with a strong long-range interaction tend to possess a strong short-range interaction. On the left lower side of the figure, the group III–V and the group II–VI semiconductors with weak electron-phonon interactions form a cluster, and on the right upper side, the insulators

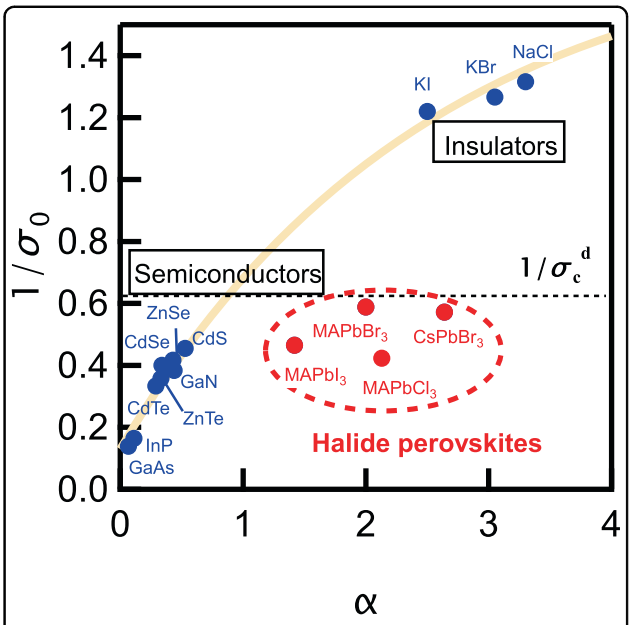

Fig. 4 The relation between the Fröhlich coupling constant and the inverse steepness parameter for various direct-gap materials. The dotted line is the theoretically predicted threshold value $1/\sigma_c^d$ for the formation of self-trapped excitons. It is expected that a self-trapped exciton is stable if $1/\sigma_0$ is larger than $1/\sigma_c^d$. Data are taken from refs. [44,45,47,52–55].

with strong electron-phonon interactions, such as alkali halides and oxides, are located. Halide perovskites do not belong to any of these clusters, and this fact clearly shows that perovskites are unusual materials from the viewpoint of electron-phonon interactions. A possible explanation for this fact would be the existence of a mechanism that enhances long-range interactions (or suppresses short-range interactions) in halide perovskites. However, it is not yet clear what leads to such an unusual behavior of halide perovskites.

Polaron formation mechanism at low temperatures

To discuss the polaron formation mechanism, it is necessary to quantitatively determine the mass enhancement due to polaron formation by experiment. For example, Landau level spectroscopy is an established technique for measuring the carrier mass. In a semiconductor under a magnetic field, Landau levels are formed by the quantization of the electron cyclotron motion (Fig. 5a). Under a magnetic field B, the optical transition between the N-th electron and hole Landau levels is observed at an energy of $E_g + E_N$, where E_g is the bandgap energy. The Landau energy E_N is

$$E_N = \left(N + \tfrac{1}{2}\right)\hbar\omega_c \quad (N = 0, 1, 2\ldots) \quad (4)$$

in the simple case without considering electron-phonon interactions. Here, the cyclotron frequency is given by

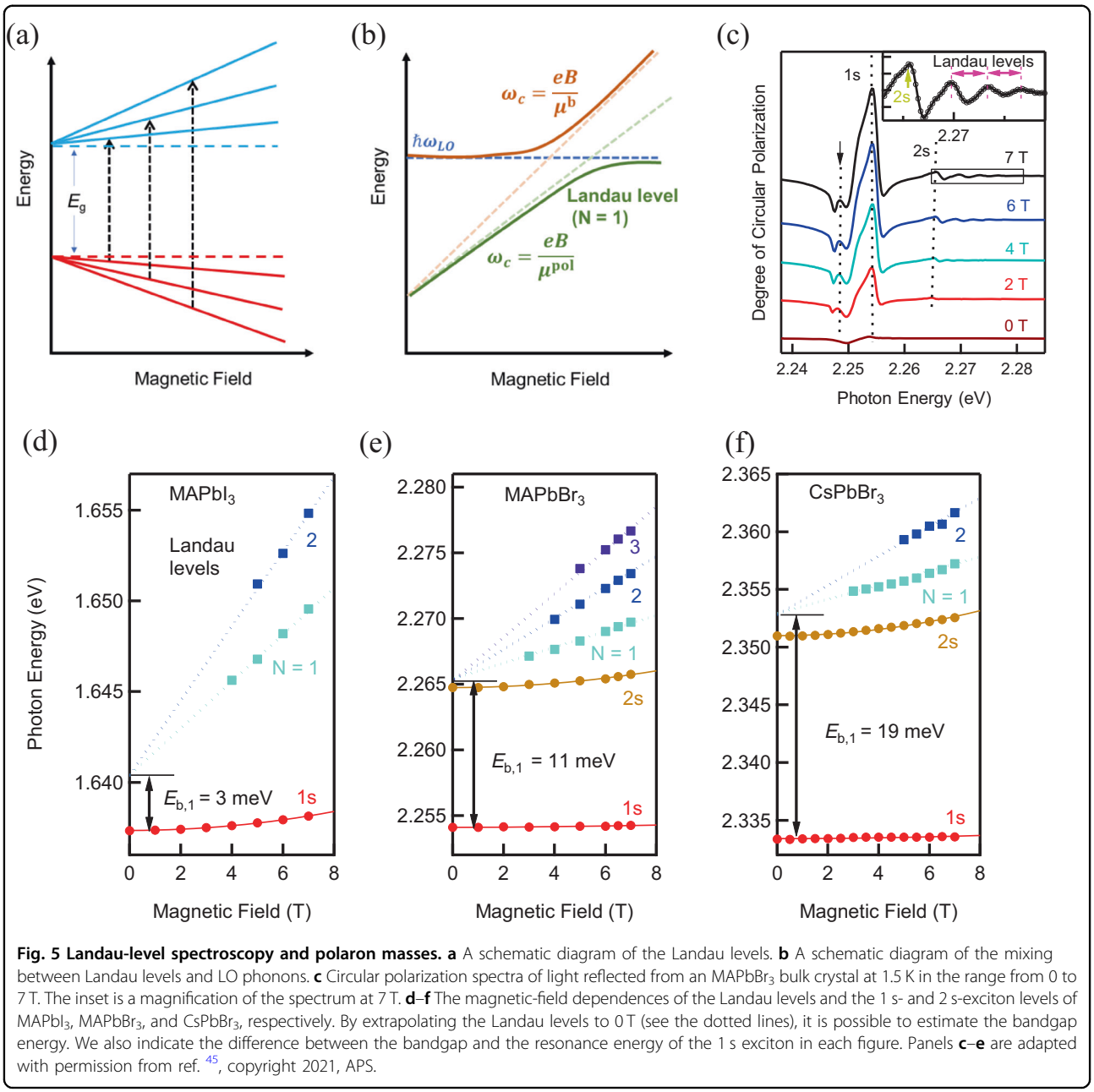

Fig. 5 Landau-level spectroscopy and polaron masses. a A schematic diagram of the Landau levels. **b** A schematic diagram of the mixing between Landau levels and LO phonons. **c** Circular polarization spectra of light reflected from an $MAPbBr_3$ bulk crystal at 1.5 K in the range from 0 to 7 T. The inset is a magnification of the spectrum at 7 T. **d**–**f** The magnetic-field dependences of the Landau levels and the 1 s- and 2 s-exciton levels of $MAPbI_3$, $MAPbBr_3$, and $CsPbBr_3$, respectively. By extrapolating the Landau levels to 0 T (see the dotted lines), it is possible to estimate the bandgap energy. We also indicate the difference between the bandgap and the resonance energy of the 1 s exciton in each figure. Panels **c**–**e** are adapted with permission from ref. [45], copyright 2021, APS.

$\omega_c = \frac{eB}{\mu^b}$, where μ^b is the band-reduced mass, which is defined by $\frac{1}{\mu^b} = \frac{1}{m_e^b} + \frac{1}{m_h^b}$. Consequently, the band-reduced mass, μ^b, can be determined from the slope of the magnetic field dependence of the Landau level energies (the so-called "Landau fan").

Strong magnetic fields are often used in Landau level spectroscopy because the Landau level signal strength becomes stronger, and the energy difference between the Landau levels becomes larger as the magnetic field increases. Therefore, performing measurements in high magnetic fields makes an easy assessment of the Landau levels possible even in samples with low quality. Miyata et al. first used magneto-spectroscopy to characterize a $MAPbI_3$ thin film[56]. The measurements were performed with magnetic fields as high as 130 T, and Landau levels were clearly observed. Other investigations of the carrier-reduced mass in lead halide perovskites by magneto-spectroscopy have also been reported[57,58].

While strong magnetic fields are helpful for observing Landau levels clearly, we should be careful to interpret the carrier-reduced mass derived from Landau spectroscopy data in the presence of strong electron-phonon interactions. In the case of the Fröhlich polaron, the phonon

becomes unable to follow the cyclotron motion of the carrier in the case of strong magnetic fields where the cyclotron frequency exceeds the LO phonon frequency. Therefore, the polaron effect vanishes at such strong magnetic fields. F. M. Peeters and J. T. Devreese considered the magnetic field dependence of the Landau levels based on the Fröhlich model[59,60]. If strong magnetic fields are present (where $E_N \gg \hbar\omega_{LO}$ is fulfilled), then the polaron effect does not appear because the phonon cannot follow the cyclotron motion. In other words, the Landau levels depend on the effective mass determined by the bare band mass. On the other hand, as shown in Fig. 5b, mixing between the Landau levels and the LO phonon energy occurs at the magnetic fields where $\hbar\omega_{LO} \cong E_N$ is fulfilled, meaning that the simple linear relation in Eq. (4) no longer holds. In the regime $\hbar\omega_{LO} \gg E_N$, the electron cyclotron motion is affected by screening due to phonons, and thus, the slope of the magnetic field dependence of the Landau level is determined by the polaron mass. Consequently, it is necessary to measure the Landau levels at sufficiently weak magnetic fields to estimate the polaron reduced mass.

Figure 5c shows differential reflectance spectra of $MAPbBr_3$ measured at different magnetic fields ($B =$ 0–7 T) at 1.5 K. In addition to the 1 s and 2 s excitons, Landau levels are apparent on the high-energy side[45]. In Fig. 5d–f, we show the magnetic field dependences of the Landau levels as well as the exciton resonance energies in $MAPbI_3$, $MAPbBr_3$, and $CsPbBr_3$ bulk crystals at 1.5 K and magnetic fields below 7 T. Because $\hbar\omega_{LO} > E_N$ holds in each material in the range below 7 T, the reduced mass derived from the Landau level energies in this magnetic field range reflects the polaron effect. If we define

$$\hbar\omega_c^*(B) = E_2(B) - E_1(B) \tag{5}$$

based on the magnetic field dependences of the Landau level energies E_1 and E_2, then the magnetic-field-dependent reduced polaron mass $\mu_{pol}(B) = eB/\omega_c^*(B)$ is approximately obtained. By extrapolating the data in Fig. 5d–f using this result, the reduced polaron masses of $MAPbI_3$, $MAPbBr_3$, and $CsPbBr_3$ at $B = 0$ T are estimated to be $\mu_{pol} = 0.13(\pm 0.01)\ m_0$, $0.20(\pm 0.01)\ m_0$, and $0.14(\pm 0.03)\ m_0$, respectively. Since the band-reduced masses estimated from the experiments at high magnetic fields are $0.104m_0$, $0.117m_0$, and $0.126m_0$[57,58], it can be considered that a mass enhancement of several tens of percent occurs due to the polaron effect, which is consistent with that determined from the Fröhlich coupling constant[45]. The above results show that the Fröhlich model can quantitatively explain polaron formation in lead halide perovskites at low temperatures. The other experiments also support the abovementioned conclusion, and we introduce two of them below.

With respect to the effective mass of a polaron, it is also possible to directly observe the band dispersion using angle-resolved photoemission spectroscopy. For example, in the case of $CsPbBr_3$, a hole polaron mass of 0.26 ($\pm$ 0.02) m_0 has been determined[61]. Considering the bare band mass determined by DFT calculations (0.17 m_0), the value of $0.26 \pm 0.02\ m_0$ constitutes an increase in the effective mass by approximately 50%. This result is also consistent with the abovementioned magneto-spectroscopy results.

The influence of the polaron effect can also be evaluated from the magnetic-field-dependent exciton resonance energy. The binding energy of the exciton in the n-th s-state is nominally given by

$$E_{b,n} = \frac{\mu^{pol} e^4}{8\varepsilon_{\text{eff}}^2 h^2} \frac{1}{n^2}. \tag{6}$$

where ε_{eff} is the effective dielectric constant, which assumes a value between ε_0 and ε_∞[62,63].

When the LO phonon energy is sufficiently large with respect to the exciton binding energy, the phonons screen the electron-hole Coulomb interaction, and ε_{eff} becomes $\cong \varepsilon_0$. Therefore, the binding energy is relatively low in such materials. Furthermore, ε_{eff} is independent of the quantum number n, and consequently, the exciton binding energy is proportional to $1/n^2$. In other words, the exciton binding energy obeys the Wannier-Mott exciton model (the hydrogen-like model). On the other hand, if the LO phonon energy is on the same order or smaller than the exciton binding energy, then the screening strength for higher-order excitons increases with the quantum number. Therefore, the Wannier-Mott exciton model does not hold. In addition, when we estimate the effective dielectric constant of the 1 s exciton by using Eq. (6) and the reduced mass, the result lies between ε_0 and ε_∞. Actually, a deviation from the Wannier model has been observed in $MAPbBr_3$, and the reported effective dielectric constant is located near the middle of ε_0 and ε_∞[45,56,57]. This result indicates that the polaron effect also influences the exciton properties. The experimentally determined exciton binding energy also agrees well with a Haken model calculation, which considers the exciton binding energy based on the Fröhlich mechanism[45].

In Fig. 6, we provide an overview of the Landau level energies and average LO phonon energies at cryogenic temperatures that have been reported for various lead halide perovskites. The yellow bars (E_N^{high}) in this figure show the energy regions of the Landau levels with $N \geq 1$ that were observed in experiments at high magnetic fields (above a few tens of Tesla[57,58]). The green bars (E_N^{low}) correspond to the Landau level energies at low magnetic fields (below 7 T) derived from the data shown in Fig. 5d–f. In the measurements at high magnetic fields, the slope of the magnetic-field dependence of the Landau level energy

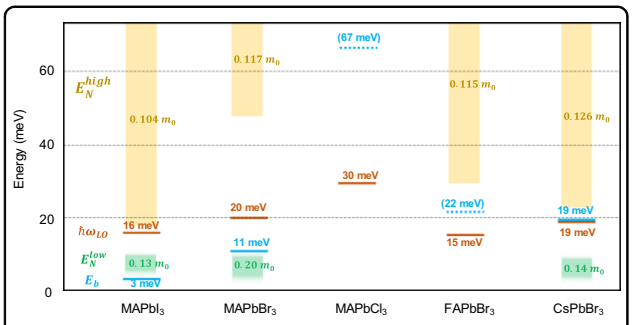

Fig. 6 Overview of Landau level energy, LO phonon energy, and exciton binding energy. The ranges of the Landau level energy determined at high (E_N^{high}) and low magnetic fields (E_N^{low}), the average LO phonon energies ($\hbar\omega_{LO}$)[40], and the exciton binding energies (E_b) of $MAPbX_3$ (X = I, Br, and Cl), $FAPbBr_3$, and $CsPbBr_3$. The Landau level data for high magnetic fields are from[57,58], and the low-magnetic-field data are from Fig. 5. The exciton binding energies of $MAPbCl_3$ and $FAPbBr_3$ were determined using the assumption of the Wannier model[45,57], and this corresponds to the upper limit of the binding energy.

provides the bare reduced mass because the Landau level energy exceeds the LO phonon energy $\hbar\omega_{LO}$, as indicated in the figure. On the other hand, under low magnetic fields, the Landau energy reflects the polaron mass. The numbers in the yellow and green bars in the figure are the reduced masses estimated from the high- or low-magnetic-field data, respectively. Compared to the results of the experiments at high magnetic fields, the reduced masses determined at low magnetic fields are larger, which is a result of the polaron effect.

As explained above, at least at cryogenic temperatures, polaron formation in halide perovskites can be quantitatively explained by the Fröhlich mechanism. This shows that the other contributions, such as small polarons or ferroelectric large polarons, are not crucial in the low-temperature phases.

Carrier mobility

Background

Among the material properties influenced by electron-phonon interactions and polaron formation, carrier transport properties have attracted the most interest. Investigations of the mechanism that governs the carrier mobility in halide perovskites are significant because the room-temperature carrier mobilities reported for various lead halide perovskites are a few to a few hundreds of cm^2/Vs[64–90]. Thus, they are 2–3 orders of magnitude smaller than high-quality inorganic semiconductors (for example, GaAs has an electron mobility of ~9000 cm^2/Vs[91]). Since the effective masses of the electron and the hole in lead halide perovskites are approximately 0.1 m_0 (and thus are not much different from conventional inorganic semiconductors), the polaron effect has frequently been considered the origin of the low mobility.

With respect to halide perovskites, which are materials with a strong ionic character, it is expected that the contribution of polar optical phonon scattering due to the Fröhlich mechanism is dominant. Several theoretical investigations based on the Fröhlich mechanism have suggested that the low optical phonon energies in perovskites are the reason for their low carrier mobilities;[15–17] a small LO phonon energy implies that many phonons are excited at room temperature, and therefore, strong scattering occurs. These theoretical investigations have predicted a room-temperature mobility of approximately 50–200 cm^2/Vs in $MAPbI_3$[15–17].

Even though polar optical phonons play a dominant role in the scattering process, the prediction of perovskite mobility near room temperature based on a simple Fröhlich-like polaron model is questionable for several reasons. One important reason is that the polaron quasiparticle picture is not always applicable at high temperatures. To understand this, we need to consider the LO phonon involved in polaron formation. As Mishchenko et al. pointed out, in the temperature regime where the energy of the LO phonon becomes larger than the thermal energy k_BT, a violation of the Mott-Ioffe-Regel criterion occurs, leading to an "undressing" of the polaron[92]. Such a condition is satisfied at room temperature because of the low phonon energies of halide perovskites. Therefore, it is most likely that the actual carrier mobility is different from the mobility predicted by the simple Fröhlich polaron model. In addition, there is the possibility that the overdamping of phonon modes or a liquid-like Debye relaxation in the GHz regime in halide perovskites also affects mobility at high temperatures[19–21,23].

Issues in the measurement of room-temperature mobility

In this context, estimating accurate carrier mobility by experiment is indispensable for discussing the polaron formation process. In Table 1, we provide an overview of the values of the carrier mobilities reported thus far for $MAPbX_3$ (X = I, Br, and Cl) bulk crystals. The reported values are scattered over a very wide range. For example, in the case of $MAPbBr_3$ single crystals, the reported values range from 0.6 to as high as 710 cm^2/Vs. These results suggest that the mobility measurements are strongly influenced by the sample quality, morphology, or the characteristics of the measurement method, suggesting difficulties in evaluating the intrinsic carrier mobility of halide perovskites. The mobility in these materials has been characterized by Hall measurements, time-of-flight measurements, and space-charge-limited current measurements. It should be considered that the unique characteristics of halide perovskites (such as mobile ions or shallow traps, high resistivity, and grain or domain boundaries) can prevent an accurate evaluation of the

Table 1 Reported carrier mobilities in $MAPbX_3$ (X = I, Br, and Cl) bulk crystals.

Material	Method	Type	Mobility (cm^2/)	Carrier density (cm^{-3})	References
$MAPbI_3$	Hall	h	105	9×10^9	64
	TOF	e	135(±20)		65
		h	90(±20)		65
		h	24		64
	SCLC	h	164		64
		h	67		66
		h	2.5		67
		e	1.16		68
		h	410		69
	THz	e,h	600		70
	Microwave	e,h	115		71
$MAPbBr_3$	Hall	h	60	-	72
		h	20–60	$5 \times 10^9 - 5 \times 10^{10}$	67
	(1% Bi doping)	e	48	2.3×10^{12}	73
		h	20–60	3.9×10^9–7.5×10^9	74
		h	37–165	$3.4 \pm 1.9 \times 10^{10}$	75
		h	30–55	5×10^{10}–3×10^{11}	76
	(AC photo Hall)	h	87	-	77
	(15% Bi doping)	e	7.51	5×10^{14}	78
		h	0.58	1.19×10^{11}	78
	(AC photo Hall)	e	318	1.8×10^{13}	79
		h	322	1.8×10^{13}	79
	TOF	h	115		67
		e	140		80
		h	220		80
		e	24.6		81
		h	59.7		81
		h	162 ± 17		77
	SCLC	h	24		66
		h	24–38		67
		h	206–217		82
		e	190		82
		e	40.7		75
		h	27.3		76
		h	81 ± 5		83
		e	41		76
		h	17.8		84
		h	47		69
		e	12.9		85
		e	13		86
	PL	e,h	310, 820		87
		e,h	710		88
	TR	e,h	10.8		89
$MAPbCl_3$	SCLC	h	12		69

The measurement technique and the carrier type (e: electron, h: hole) are given in the second and third columns, respectively. Note that Hall measurements also provide the carrier densities. *TOF* Time-of-flight, *SCLC* Space-charge-limited current, *TR* Transient reflectance.

mobility when these methods are applied to metal halide perovskites[81,93,94].

Below, we focus on the most established method for evaluating the carrier mobility, namely, the Hall measurement. The difficulty of Hall measurements of lead halide perovskites lies in the low carrier density. Hall measurements are usually performed at carrier densities in the range above $10^{14}\,cm^{-3}$. Note that an effective method to introduce impurities to enhance the carrier density for halide perovskites has not yet been established. For example, even with a Bi^{3+} doping amount of 1%, a low carrier density of only approximately $10^{12}\,cm^{-3}$ is activated[73]. In heavily doped samples, impurity scattering becomes dominant, making it difficult to measure the intrinsic carrier mobility. As shown in Table 1, the Hall mobilities were estimated at low carrier densities of 10^9 to $10^{11}\,cm^{-3}$ except for the Bi-doped samples. In the case of such low carrier densities, it is not easy to evaluate the Hall mobilities with high accuracy by conventional Hall measurements. In addition, in the low carrier density region, scattering processes that originate from impurities (such as dislocation scattering) can become dominant, and then the intrinsic carrier mobility is no longer accessible. Interestingly, in heavily doped $MASnI_3$ single crystals where self-doping by Sn^{4+} occurs, a high carrier density of $10^{14}\,cm^{-3}$ has been realized, and mobilities exceeding $2000\,cm^2/Vs$ have been reported[95,96]. As plotted in Fig. 7a, Sn-based halide perovskites tend to exhibit higher mobility than Pb-based perovskites. This result suggests that carrier density is a key parameter in evaluating the intrinsic carrier mobility in metal halide perovskites.

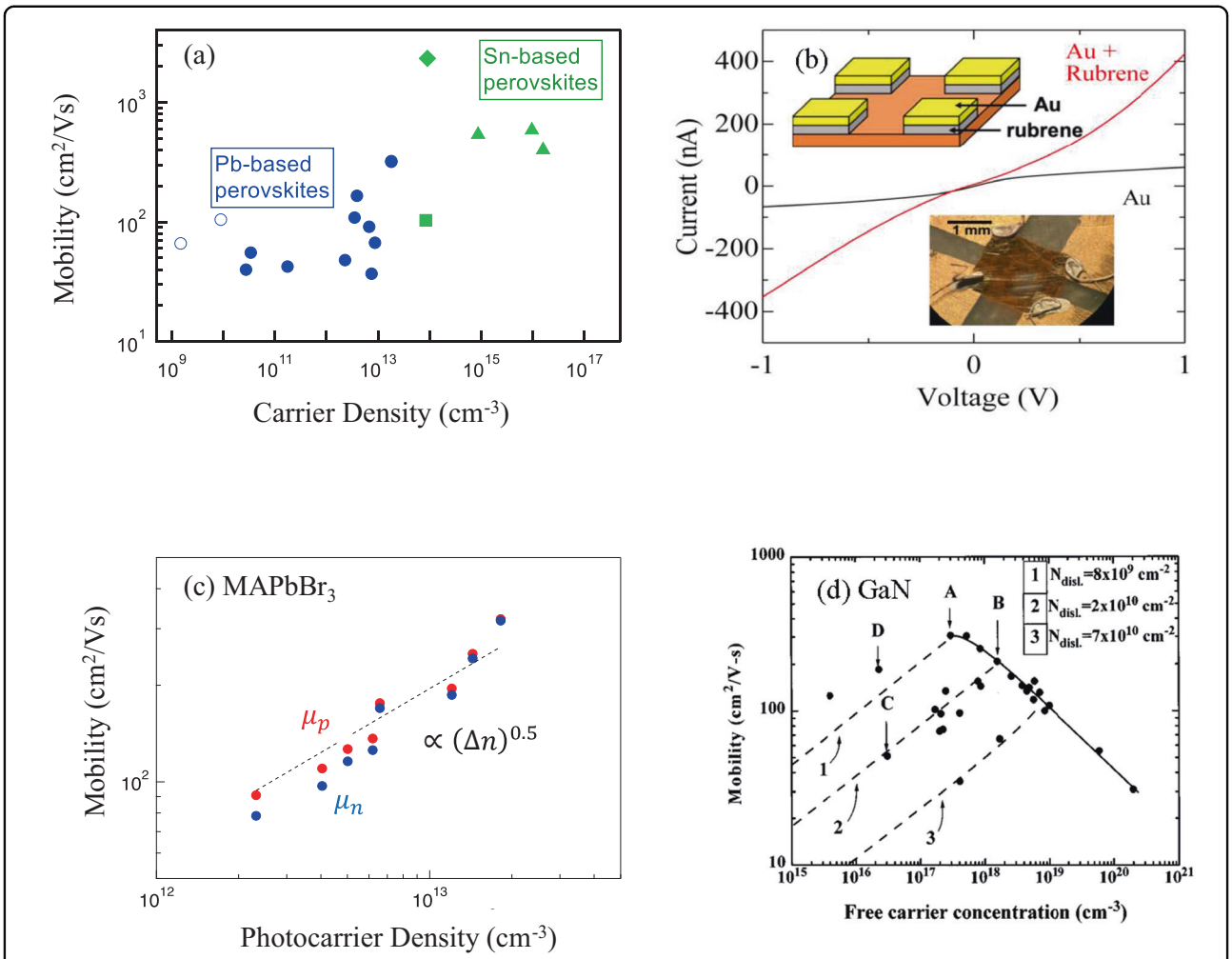

Fig. 7 Hall mobilities of carriers in halide perovskites. a Reported Hall mobility of Pb- and Sn-based halide perovskites. (filled circle: $MAPbBr_3$;[67,72–79] open circle: $MAPbI_3$;[66] filled square: $FASnI_3$;[95] filled diamond: $MASnI_3$;[95] filled triangle: $CsSnI_3$[95,96]) **b** The sample used in the AC photo-Hall measurement and the I–V curves with and without the rubrene interlayer. **c** Electron and hole mobilities in $MAPbBr_3$ as a function of the photocarrier density[79]. **d** Dependence of the carrier mobility on the carrier density in GaN samples with different dislocation defect densities. Panels **b**, **c** are adapted from ref. [79], licensed under CC BY 4.0. Panel **d** is adapted with permission from ref. [98], copyright 1998, AIP.

AC photo-Hall measurements

In samples where the carrier doping technique is not established, photodoping is an effective method to increase the carrier density. In simple Hall measurements under illumination, only the difference between the electron and hole mobilities can be obtained. However, Gunawan et al. developed a method that allowed us to determine the electron and hole mobilities independently from the excitation-density dependence. These researchers demonstrated the estimation of electron and hole mobilities in a perovskite thin film by AC photo-Hall measurements[97].

We recently measured the electron and hole mobilities by applying the AC photo-Hall measurement method to a $MAPbBr_3$ bulk single crystal[79]. In this experiment, we tried to determine the intrinsic mobilities by incorporating experimental refinements, such as using a thinned, high-quality single crystal, reducing the contact resistance of the electrode by inserting a rubrene layer, and applying uniform near-band-edge excitation (Fig. 7b). In Fig. 7c, we plot the estimated electron and hole mobilities as a function of the photoexcited carrier density. We find that the carrier mobility increases with the carrier density. A similar carrier density dependence was also reported by Musiienko et al.[77]. In materials such as GaN and Ge, carrier mobilities depending on carrier density due to dislocation scattering have been reported in the low carrier density region[98], similar to those observed in $MAPbBr_3$ (Fig. 7d). Consequently, the mobility in $MAPbBr_3$ in the low carrier density regime might be suppressed by extrinsic carrier scattering processes such as dislocation scattering. In other words, it is suggested that the realization of a high carrier density may

have found the intrinsic carrier mobility of halide perovskite. It is also interesting that a high mobility exceeding 300 cm^2/Vs has been obtained by photoluminescence (PL) dynamics measurements under intense femtosecond-laser excitation[87,88]. This result is consistent with the excitation-intensity dependence of the carrier mobility determined from the AC photo-Hall measurement.

As shown in Fig. 7c, at the highest photocarrier density in this experiment, the carrier mobility exceeds 300 cm^2/Vs. This value is of the same order as the highest electron mobilities of the group II–VI semiconductors that possess a bandgap energy similar to that of $MAPbBr_3$ (i.e., CdS with 385 cm^2/Vs, CdSe with 605 cm^2/Vs, and ZnSe with 530 cm^2/Vs)[99]. This result indicates that halide perovskites also have considerable potential as electronic device materials.

Notably, this value of 300 cm^2/Vs exceeds the upper limit of the carrier mobility reported in theoretical investigations based on the Fröhlich polaron model (50–212 cm^2/Vs)[15–17]. This result implies that the simple Fröhlich polaron model cannot accurately predict the room-temperature mobilities in lead halide perovskites. As mentioned above, an undressing polaron occurs in perovskites at room temperature, and thus, the Fröhlich polaron quasiparticle picture fails. It is considered that the carrier mobility can become larger than that derived using the polaron picture[92]. Moreover, there is the possibility that an overdamped phonon weakens the polaron effect[40].

The high carrier mobility estimated in the AC photo-Hall measurement suggests that influences such as those of dynamical disorder or ferroelectric large polarons are limited. However, a physical model that can quantitatively characterize these effects on mobility has not yet been established. In addition to the quantitative evaluation of the mobilities in various halide perovskites, it is necessary to develop a physical model that accounts for the abovementioned deviations from the Fröhlich polaron model and the influence of the overdamped phonon due to phonon anharmonicity.

Examples of the impact of electron-phonon interactions on other properties

The electron-phonon interactions can also significantly affect the optical band-edge properties and the carrier relaxation dynamics. Here, we introduce unique optical properties and relaxation dynamics arising from electron-phonon interactions.

Anti-Stokes photoluminescence (PL)

Anti-Stokes PL is the luminescence at energies higher than the photon energy of the excitation light. In semiconductors, anti-Stokes PL can be generated when phonon-assisted photoabsorption occurs at energies slightly below the bandgap energy (Fig. 8a). As shown in Fig. 8b, an anti-Stokes PL is observed in $MAPbI_3$ when the Urbach tail below the bandgap energy is excited[25]. This figure also shows that the PL spectrum is independent of the excitation energy, which means that the PL linewidth is determined by homogeneous broadening. As shown in Fig. 4, halide perovskites possess a steepness parameter that is lower than that of conventional semiconductors. Therefore, halide perovskites exhibit a large intrinsic Urbach tail, which can be advantageous for anti-Stokes PL via phonon absorption. Furthermore, the steepness parameter is even higher than the threshold for self-trapped exciton formation. This is important because forming a self-trapped exciton would lead to PL with lower photon energy and thus would reduce the anti-Stokes effect (which is to obtain high-energy photons).

Such an anti-Stokes PL is also considered highly useful for the realization of solid-state laser cooling: If the anti-Stokes PL efficiency is sufficiently close to 100%, then the

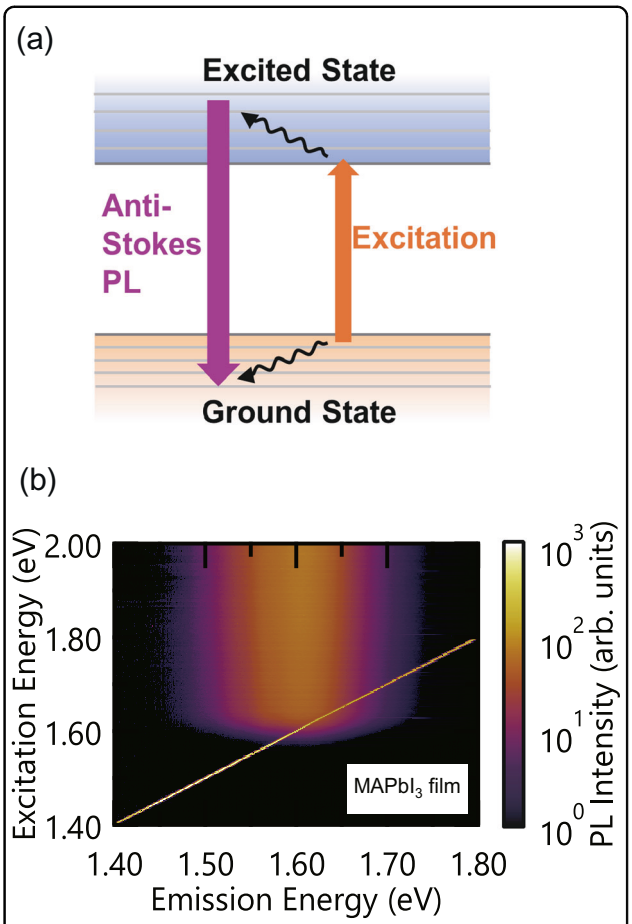

Fig. 8 Anti-Stokes PL from halide perovskites. a Schematic illustration of anti-Stokes PL via phonon absorption in a semiconductor. **b** PL excitation map of a $MAPbI_3$ thin film. The thin diagonal line corresponds to the scattering signal of the excitation light. Panel b is adapted with permission from ref. [25], licensed under CC BY 4.0.

energy emitted by luminescence becomes larger than the energy received by the material from the excitation light. Therefore, the material is subject to cooling in this case[100]. Such optical cooling has been investigated intensively in rare-earth-doped crystals and glasses[101,102], but optical cooling in semiconductors with strong optical absorption has large possibilities that are not yet fully exploited[103,104].

Slow relaxation of hot carriers

If a semiconductor is excited using an excitation photon energy that largely exceeds the bandgap energy, then carriers with excess energy, so-called hot carriers, are generated. When the excess energy of a hot carrier is sufficiently large, it is usually considered that the relaxation of the hot carrier occurs by the interaction with optical phonons (that is, by the Fröhlich interaction). However, with respect to halide perovskites, a relatively slow hot-carrier relaxation has been reported in several studies[26,105]. In other words, the relaxation time constant is significantly longer than that in conventional inorganic semiconductors. Several mechanisms, such as a hot-phonon bottleneck, acoustic-optical phonon upconversion, Auger heating, band-filling, and large polaron formation, have been proposed as possible origins of such a long relaxation time.

To shed more light on the origin of the slow relaxation of hot carriers, Sekiguchi et al. investigated the change in the PL dynamics induced by pulsed THz excitation of an $MAPbI_3$ film, as shown in Fig. 9[27]. Here, the THz pulse was tuned to the transverse optical (TO) phonon resonance, and thus, THz excitation can be used to intentionally alter the phonon population in the sample, which also affects the carrier relaxation and distribution. Figure 9b shows that the total PL intensity decreases immediately after THz excitation. Simultaneously, the PL intensity on the high-energy side slightly increases (not shown here). The PL intensity recovers within a few tens of picoseconds. These results mean that a hot-phonon bottleneck determines the relaxation process. In other words, the TO phonons generated by THz excitation are quickly converted into LO phonons because of the strong phonon anharmonicity in this material. Due to a large amount of generated LO phonons, the relaxation path that emits LO phonons is restricted, leading to the reduction in the PL (see Fig. 9). The control of the hot-carrier relaxation pathways will be expected to be utilized for unique applications such as hot-carrier solar cells[106].

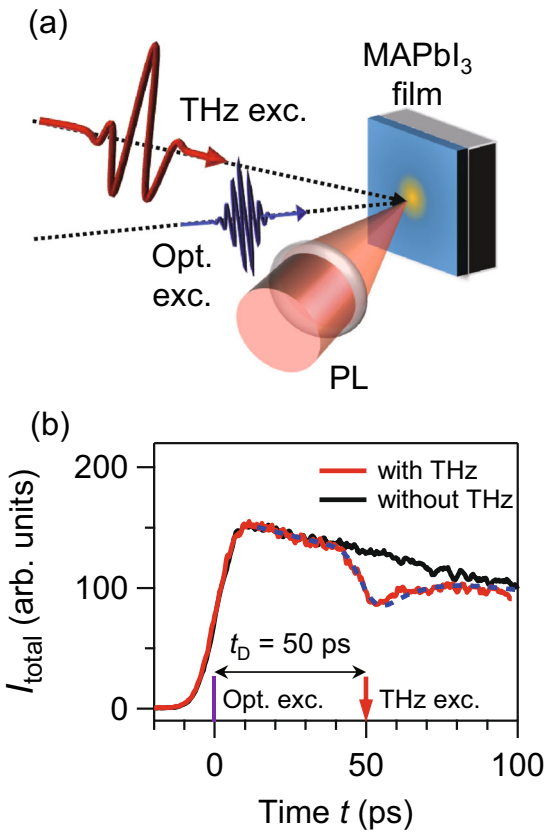

Fig. 9 Hot carrier cooling process revealed by THz pump-optical probe experiments. a Schematic of the pump–probe experiment to verify the influence of the phonon population on the carrier relaxation. **b** Result of the pump–probe experiment with and without the THz pulse. The broken curve shows the theoretical prediction. Adapted with permission from ref. [27], licensed under CC BY 4.0.

Summary and outlook

In this review, we have discussed important aspects of the optical and electrical properties caused by electron-phonon interactions in metal halide perovskites. The Fröhlich-type electron-phonon interactions in lead halide perovskites are considerably larger than those in conventional inorganic semiconductors, which is a factor of their unique physical properties. As can be understood from magneto-spectroscopy, polaron formation due to the Fröhlich interaction is dominant at low temperatures because of the ionic nature of perovskite crystals. However, we need to consider that it is difficult to explain the polaron formation at room temperature only by the simple Fröhlich model. To advance our understanding of the role of electron-phonon interactions, it will become important to consider the deviation from the Fröhlich polaron model at room temperature and consider other polaron formation mechanisms. An accurate evaluation of the carrier mobility is essential for this task, but halide perovskites are materials where achieving high carrier densities by doping is still difficult. As explained in this review, we can estimate the carrier mobility under photodoping conditions by using an AC photo-Hall measurement, and mobilities higher than those obtained in conventional Hall measurements have been observed.

This result suggests that halide perovskites not only have a high potential for use in optical devices but also have a high potential for use in electronic devices. To gain a deeper understanding of the carrier transport properties, clarifying the carrier scattering mechanisms in the high-carrier-density regime will be necessary.

While electron-phonon interactions in metal halide perovskites can result in a reduction in mobility or induce ion migration and thus partially constitute a harmful factor in device applications, they also lead to slow relaxation of hot carriers as well as anti-Stokes PL, and the utilization of these unique phenomena in new devices is expected.

Acknowledgements
The authors would like to thank many colleagues for their contributions and useful discussions. The authors gratefully acknowledge M. Nagai, T. Yamada, and T. Kimura for their support. Part of this work was supported by JST-CREST (JPMJCR16N3), JSPS KAKENHI (JP19K03683, JP19H05465), the Canon Foundation, and the Chiba Iodine Resource Innovation Center.

Author contributions
All authors wrote the manuscript.

Conflict of interest
The authors declare no competing interests.

Received: 20 December 2021 Revised: 24 March 2022 Accepted: 29 March 2022.
Published online: 3 June 2022

References

1. Kojima, A., Teshima, K., Shirai, Y. & Miyasaka, T. Organometal halide perovskites as visible-light sensitizers for photovoltaic cells. *J. Am. Chem. Soc.* **131**, 6050–6051 (2009).
2. Tan, Z. K. et al. Bright light-emitting diodes based on organometal halide perovskite. *Nat. Nanotechnol.* **9**, 687–692 (2014).
3. Stranks, S. D. et al. Electron-hole diffusion lengths exceeding 1 micrometer in an organometal trihalide perovskite absorber. *Science* **342**, 341–344 (2013).
4. Xing, G. et al. Long-range balanced electron- and hole-transport lengths in organic-inorganic $CH_3NH_3PbI_3$. *Science* **347**, 344–347 (2013).
5. Yamada, Y., Nakamura, T., Endo, M., Wakamiya, A. & Kanemitsu, Y. Photocarrier recombination dynamics in perovskite $CH_3NH_3PbI_3$ for solar cell applications. *J. Am. Chem. Soc.* **136**, 11610–11613 (2014).
6. Yamada, Y. et al. Dynamic optical properties of $CH_3NH_3PbI_3$ single crystals as revealed by one-and two-photon excited photoluminescence measurements. *J. Am. Chem. Soc.* **137**, 10456–10459 (2015).
7. Handa, T., Yamada, T., Nagai, M. & Kanemitsu, Y. Phonon, thermal, and thermo-optical properties of halide perovskites. *Phys. Chem. Chem. Phys.* **22**, 26069–26087 (2020).
8. Tahara, H., Aharen, T., Wakamiya, A. & Kanemitsu, Y. Photorefractive effect in organic–inorganic hybrid perovskites and its application to optical phase shifter. *Adv. Opt. Mater.* **6**, 1701366 (2018).
9. Wu, L. et al. Perovskite $CsPbX_3$: A promising nonlinear optical material and its applications for ambient all-optical switching with enhanced stability. *Adv. Opt. Mater.* **6**, 1800400 (2018).
10. Hirori, H. et al. High-order harmonic generation from hybrid organic–inorganic perovskite thin films. *APL Mater.* **7**, 041107 (2019).
11. Jang, D. M. et al. Reversible halide exchange reaction of organometal trihalide perovskite colloidal nanocrystals for full-range band gap tuning. *Nano Lett.* **15**, 5191 (2015).
12. Rakita, Y., Cohen, S. R., Kedem, N. K., Hodes, G. & Cahen, D. Mechanical properties of $APbX_3$ (A= Cs or CH_3NH_3; X= I or Br) perovskite single crystals. *MRS Commun.* **5**, 623–629 (2015).
13. Jung, H. S., Han, G. S., Park, N. G. & Ko, M. J. Flexible perovskite solar cells. *Joule* **3**, 1850–1880 (2019).
14. Franchini, C., Reticcioli, M., Setvin, M. & Diebold, U. Polarons in materials. *Nat. Rev. Mater.* **6**, 560–586 (2021).
15. Sendner, M. et al. Optical phonons in methylammonium lead halide perovskites and implications for charge transport. *Mater. Horiz.* **3**, 613–620 (2016).
16. Frost, J. M. Calculating polaron mobility in halide perovskites. *Phys. Rev. B* **96**, 195202 (2017).
17. Poncé, S., Schlipf, M. & Giustino, F. Origin of low carrier mobilities in halide perovskites. *ACS Energy Lett.* **4**, 456–463 (2019).
18. Miyata, K. et al. Large polarons in lead halide perovskites. *Sci. Adv.* **3**, e1701217 (2017).
19. Yaffe, O. et al. Local polar fluctuations in lead halide perovskite crystals. *Phys. Rev. Lett.* **118**, 136001 (2017).
20. Miyata, K. & Zhu, X. Y. Ferroelectric large polarons. *Nat. Mater.* **17**, 379–381 (2018).
21. Guo, Y. et al. Dynamic emission Stokes shift and liquid-like dielectric solvation of band edge carriers in lead-halide perovskites. *Nat. Commun.* **10**, 1175 (2019).
22. Meggiolaro, D., Ambrosio, F., Mosconi, E., Mahata, A. & De Angelis, F. Polarons in metal halide perovskites. *Adv. Energy Mater.* **10**, 1902748 (2020).
23. Ghosh, D., Welch, E., Neukirch, A. J., Zakhidov, A. & Tretiak, S. Polarons in halide perovskites: A perspective. *J. Phys. Chem. Lett.* **11**, 3271–3286 (2020).
24. Schilcher, M. J. et al. The significance of polarons and dynamic disorder in halide perovskites. *ACS Energy Lett.* **6**, 2162–2173 (2021).
25. Yamada, T., Aharen, T. & Kanemitsu, Y. Up-converted photoluminescence from $CH_3NH_3PbI_3$ perovskite semiconductors: Implications for laser cooling. *Phys. Rev. Mater.* **3**, 024601 (2019).
26. Li, M., Fu, J., Xu, Q. & Sum, T. C. Slow hot-carrier cooling in halide perovskites: Prospects for hot-carrier solar cells. *Adv. Mater.* **31**, 1802486 (2019).
27. Sekiguchi, F. et al. Enhancing the hot-phonon bottleneck effect in a metal halide perovskite by terahertz phonon excitation. *Phys. Rev. Lett.* **126**, 077401 (2021).
28. Yang, Y. et al. Observation of a hot-phonon bottleneck in lead-iodide perovskites. *Nat. Photon* **10**, 53–59 (2016).
29. Yamada, Y., Endo, M., Wakamiya, A. & Kanemitsu, Y. Spontaneous defect annihilation in $CH_3NH_3PbI_3$ thin films at room temperature revealed by time-resolved photoluminescence spectroscopy. *J. Phys. Chem. Lett.* **6**, 482–486 (2015).
30. Nie, W. et al. Light-activated photocurrent degradation and self-healing in perovskite solar cells. *Nat. Commun.* **7**, 11574 (2016).
31. Mahata, A., Meggiolaro, D. & De Angelis, F. From large to small polarons in lead, tin, and mixed lead–tin halide perovskites. *J. Phys. Chem. Lett.* **10**, 1790–1798 (2019).
32. Li, Z. et al. Stabilizing perovskite structures by tuning tolerance factor: formation of formamidinium and cesium lead iodide solid-state alloys. *Chem. Mater.* **28**, 284–292 (2016).
33. Poglitsch, A. & Weber, D. Dynamic disorder in methylammonium-trihalogenoplumbates (II) observed by millimeter-wave spectroscopy. *J. Chem. Phys.* **87**, 6373–6378 (1987).
34. Onoda-Yamamuro, N., Matsuo, T. & Suga, H. Dielectric study of $CH_3NH_3PbX_3$ (X = Cl, Br, I). *J. Phys. Chem. Solids* **53**, 935–939 (1992).
35. Yamada, Y., Yamada, T. & Kanemitsu, Y. Free carrier radiative recombination and photon recycling in lead halide perovskite solar cell materials. *Bull. Chem. Soc. Jpn.* **90**, 1129–1140 (2017).
36. Marronnier, A. et al. Anharmonicity and disorder in the black phases of cesium lead iodide used for stable inorganic perovskite solar cells. *ACS nano* **12**, 3477–3486 (2018).
37. Quarti, C. et al. The Raman spectrum of the $CH_3NH_3PbI_3$ hybrid perovskite: interplay of theory and experiment. *J. Phys. Chem. Lett.* **5**, 279–284 (2013).
38. La-o-Vorakiat, C. et al. Phonon mode transformation across the orthohombic–tetragonal phase transition in a lead iodide perovskite $CH_3NH_3PbI_3$: a terahertz time-domain spectroscopy approach. *J. Phys. Chem. Lett.* **7**, 1–6 (2016).

39. Leguy, A. M. et al. Dynamic disorder, phonon lifetimes, and the assignment of modes to the vibrational spectra of methylammonium lead halide perovskites. *Phys. Chem. Chem. Phys.* **18**, 27051–27066 (2016).
40. Nagai, M. et al. Longitudinal optical phonons modified by organic molecular cation motions in organic-inorganic hybrid perovskites. *Phys. Rev. Lett.* **121**, 145506 (2018).
41. Ferreira, A. C. et al. Direct evidence of weakly dispersed and strongly anharmonic optical phonons in hybrid perovskites. *Commun. Phys.* **3**, 48 (2020).
42. Fröhlich, H. Electrons in lattice fields. *Adv. Phys.* **3**, 325–361 (1954).
43. Röseler, J. A new variational ansatz in the polaron theory. *Phys. Status Solidi (b)* **25**, 311 (1968).
44. Devreese, J. T. in Encyclopedia of Physics. 2 3rd edn (eds Lerner, R. G. & Trigg, G. L.) 2004-2027 (Wiley-VCH, Berlin, Germany, 2005).
45. Yamada, Y. et al. Polaron masses in $CH_3NH_3PbX_3$ perovskites determined by landau level spectroscopy in low magnetic fields. *Phys. Rev. Lett.* **126**, 237401 (2021).
46. Sumi, H. & Toyozawa, Y. Urbach-Martienssen rule and exciton trapped momentarily by lattice vibrations. *J. Phys. Soc. Jpn.* **31**, 342–358 (1971).
47. Toyozawa, Y. *Optical Processes in Solids* (Cambridge University Press, Cambridge, UK, 2003).
48. Neukirch, A. J. et al. Polaron stabilization by cooperative lattice distortion and cation rotations in hybrid perovskite materials. *Nano Lett.* **16**, 3809–3816 (2016).
49. Cody, G. D., Tiedje, T., Abeles, B., Brooks, B. & Goldstein, Y. Disorder and the optical-absorption edge of hydrogenated amorphous silicon. *Phys. Rev. Lett.* **47**, 1480 (1981).
50. Yamada, Y., Nakamura, T., Endo, M., Wakamiya, A. & Kanemitsu, Y. Near-band-edge optical responses of solution-processed organic–inorganic hybrid perovskite $CH_3NH_3PbI_3$ on mesoporous TiO_2 electrodes. *Appl. Phys. Express* **7**, 032302 (2014).
51. Yamada, T., Handa, T., Yamada, Y. & Kanemitsu, Y. Light emission from halide perovskite semiconductors: bulk crystals, thin films, and nanocrystals. *J. Phys. D: Appl. Phys.* **54**, 383001 (2021).
52. Yamada, T., Aharen, T. & Kanemitsu, Y. Near-band-edge optical responses of $CH_3NH_3PbCl_3$ single crystals: photon recycling of excitonic luminescence. *Phys. Rev. Lett.* **120**, 057404 (2018).
53. Wolf, C., Kim, J. S. & Lee, T. W. Structural and thermal disorder of solution-processed $CH_3NH_3PbBr_3$ hybrid perovskite thin films. *ACS Appl. Mater. Interfaces* **9**, 10344–10348 (2017).
54. Ledinsky, M. et al. Temperature dependence of the urbach energy in lead iodide perovskites. *J. Phys. Chem. Lett.* **10**, 1368–1373 (2019).
55. Kajino, Y. et al. Anti-Stokes Photoluminescence from $CsPbBr_3$ Nanostructures Embedded in a Cs_4PbBr_6 Crystal. *Phys. Rev. Mater.* **6**, L043001 (2022).
56. Miyata, A. et al. Direct measurement of the exciton binding energy and effective masses for charge carriers in organic–inorganic tri-halide perovskites. *Nat. Phys.* **11**, 582–587 (2015).
57. Galkowski, K. et al. Determination of the exciton binding energy and effective masses for methylammonium and formamidinium lead tri-halide perovskite semiconductors. *Energy Environ. Sci.* **9**, 962–970 (2016).
58. Yang, Z. et al. Impact of the halide cage on the electronic properties of fully inorganic cesium lead halide perovskites. *ACS Energy Lett.* **2**, 1621–1627 (2017).
59. Peeters, F. M. & Devreese, J. T. Energy levels of two-and three-dimensional polarons in a magnetic field. *Phys. Rev. B* **31**, 3689 (1985).
60. Peeters, F. M. & Devreese, J. T. Magneto-optical absorption of polarons. *Phys. Rev. B* **34**, 7246 (1986).
61. Puppin, M. et al. Evidence of large polarons in photoemission band mapping of the perovskite semiconductor $CsPbBr_3$. *Phys. Rev. Lett.* **124**, 206402 (2020).
62. Haken, H. Zur quantentheorie des mehrelektronensystems im schwingenden gitter. *Z. Phys.* **146**, 527–554 (1956).
63. Klingshirn, C. F. *Semiconductor Optics* 4th edn (Springer, Berlin, Germany, 2012).
64. Dong, Q. et al. Electron-hole diffusion lengths> 175 μm in solution-grown CH3NH3PbI3 single crystals. *Science* **347**, 967–970 (2015).
65. Shrestha, S. et al. Assessing temperature dependence of drift mobility in methylammonium lead iodide perovskite single crystals. *J. Phys. Chem. C.* **122**, 5935–5939 (2018).
66. Saidaminov, M. I. et al. High-quality bulk hybrid perovskite single crystals within minutes by inverse temperature crystallization. *Nat. Commun.* **6**, 7586 (2015).
67. Shi, D. et al. Low trap-state density and long carrier diffusion in organolead trihalide perovskite single crystals. *Science* **347**, 519–522 (2015).
68. Song, Y. et al. Efficient lateral-structure perovskite single crystal solar cells with high operational stability. *Nat. Commun.* **11**, 274 (2020).
69. Bari, M. et al. Room-temperature synthesis, growth mechanisms and opto-electronic properties of organic–inorganic halide perovskite $CH_3NH_3PbX_3$ (X = I, Br, and Cl) single crystals. *CrystEngComm.* **23**, 3326–3339 (2021).
70. Valverde-Chávez, D. A. et al. Intrinsic femtosecond charge generation dynamics in single crystal $CH_3NH_3PbI_3$. *Energy Environ. Sci.* **8**, 3700–3707 (2015).
71. Semonin, O. E. et al. Limits of carrier diffusion in n-type and p-type $CH_3NH_3PbI_3$ perovskite single crystals. *J. Phys. Chem. Lett.* **7**, 3510–3518 (2016).
72. Chen, Y. et al. Extended carrier lifetimes and diffusion in hybrid perovskites revealed by Hall effect and photoconductivity measurements. *Nat. Commun.* **7**, 12253 (2016).
73. Yamada, Y., Hoyano, M., Akashi, R., Oto, K. & Kanemitsu, Y. Impact of chemical doping on optical responses in bismuth-doped $CH_3NH_3PbBr_3$ single crystals: carrier lifetime and photon recycling. *J. Phys. Chem. Lett.* **8**, 5798–5803 (2017).
74. Wang, Q. et al. Morphological and chemical tuning of lead halide perovskite mesocrystals as long-life anode materials in lithium-ion batteries. *CrystEngComm* **21**, 1048–1059 (2019).
75. Rao, H. S., Li, W. G., Chen, B. X., Kuang, D. B. & Su, C. Y. In situ growth of 120 cm^2 $CH_3NH_3PbBr_3$ perovskite crystal film on FTO glass for narrowband-photodetectors. *Adv. Mater.* **29**, 1602639 (2017).
76. Lin, C. H. et al. Metal contact and carrier transport in single crystalline $CH_3NH_3PbBr_3$ perovskite. *Nano Energy* **53**, 817–827 (2018).
77. Musiienko, A. et al. Deep levels, charge transport and mixed conductivity in organometallic halide perovskites. *Energy Environ. Sci.* **12**, 1413–1425 (2019).
78. Tang, W. et al. Substitutional doping of hybrid organic–inorganic perovskite crystals for thermoelectrics. *J. Mater. Chem. A* **8**, 13594–13599 (2020).
79. Kimura, T., Matsumori, K., Oto, K., Kanemitsu, Y. & Yamada, Y. Observation of high carrier mobility in $CH_3NH_3PbBr_3$ single crystals by AC photo-Hall measurements. *Appl. Phys. Express* **14**, 041009 (2021).
80. Wei, H. et al. Dopant compensation in alloyed $CH_3NH_3PbBr_{3-x}Cl_x$ perovskite single crystals for gamma-ray spectroscopy. *Nat. Mater.* **16**, 826 (2017).
81. Liu, X. et al. Charge transport behavior in solution-grown methylammonium lead tribromide perovskite single crystal using α particles. *J. Phys. Chem. C.* **122**, 14355–14361 (2018).
82. Wei, H. et al. Sensitive X-ray detectors made of methylammonium lead tribromide perovskite single crystals. *Nat. Photonics* **10**, 333–339 (2016).
83. Liu, Y. et al. A 1300 mm^2 ultrahigh-performance digital imaging assembly using high-quality perovskite single crystals. *Adv. Mater.* **30**, 1707314 (2018).
84. Pospisil, J. et al. Density of bulk trap states of hybrid lead halide perovskite single crystals: temperature modulated space-charge-limited-currents. *Sci. Rep.* **9**, 3332 (2019).
85. Duijnstee, E. A. et al. Understanding dark current-voltage characteristics in metal-halide perovskite single crystals. *Phys. Rev. Appl.* **15**, 014006 (2021).
86. Le Corre, V. M. et al. Revealing charge carrier mobility and defect densities in metal halide perovskites via space-charge-limited current measurements. *ACS Energy Lett.* **6**, 1087–1094 (2021).
87. Yamada, T. et al. Fast free-carrier diffusion in $CH_3NH_3PbBr_3$ single crystals revealed by time-resolved one-and two-photon excitation photoluminescence spectroscopy. *Adv. Electron. Mater.* **2**, 1500290 (2016).
88. Yamada, T., Yamada, Y., Nakaike, Y., Wakamiya, A. & Kanemitsu, Y. Photon emission and reabsorption processes in $CH_3NH_3PbBr_3$ single crystals revealed by time-resolved two-photon-excitation photoluminescence microscopy. *Phys. Rev. Appl.* **7**, 014001 (2017).
89. Yang, Y. et al. Low surface recombination velocity in solution-grown $CH_3NH_3PbBr_3$ perovskite single crystal. *Nat. Commun.* **6**, 7961 (2015).
90. Zhang, Z. & Saparov, B. Charge carrier mobility of halide perovskite single crystals for ionizing radiation detection. *Appl. Phys. Lett.* **119**, 030502 (2021).
91. Stillman, G. E., Waife, C. M. & Dimmock, J. O. Hall coefficient factor for polar mode scattering in n-type GaAs. *J. Phys. Chem. Solids* **31**, 1199 (1970).
92. Mishchenko, A. S. et al. Polaron mobility in the "beyond quasiparticles" regime. *Phys. Rev. Lett.* **123**, 076601 (2019).
93. Alvar, M. S., Blom, P. W. & Wetzelaer, G. J. A. Space-charge-limited electron and hole currents in hybrid organic-inorganic perovskites. *Nat. Commun.* **11**, 4023 (2020).
94. Jin, H. et al. It's a trap! On the nature of localised states and charge trapping in lead halide perovskites. *Mater. Horiz.* **7**, 397–410 (2020).

95. Stoumpos, C. C., Malliakas, C. D. & Kanatzidis, M. G. Semiconducting tin and lead iodide perovskites with organic cations: phase transitions, high mobilities, and near-infrared photoluminescent properties. *Inorg. Chem.* **52**, 9019–9038 (2013).
96. Chung, I. et al. $CsSnI_3$: semiconductor or metal? High electrical conductivity and strong near-infrared photoluminescence from a single material. High hole mobility and phase-transitions. *J. Am. Chem. Soc.* **134**, 8579–8587 (2012).
97. Gunawan, O. et al. Carrier-resolved photo-Hall effect. *Nature* **575**, 151–155 (2019).
98. Ng, H. M., Doppalapudi, D., Moustakas, T. D., Weimann, N. G. & Eastman, L. F. The role of dislocation scattering in n-type GaN films. *Appl. Phys. Lett.* **73**, 821 (1998).
99. Yang, X., Xu, C. & Giles, N. C. Intrinsic electron mobilities in CdSe, CdS, ZnO, and ZnS and their use in analysis of temperature-dependent Hall measurements. *J. Appl. Phys.* **104**, 073727 (2008).
100. Sheik-Bahae, M. & Epstein, R. I. Optical refrigeration. *Nat. Photonics* **1**, 693–699 (2007).
101. Seletskiy, D. V. et al. Laser cooling of solids to cryogenic temperatures. *Nat. Photonics* **4**, 161–164 (2010).
102. Melgaard, S. D., Albrecht, A. R., Hehlen, M. P. & Sheik-Bahae, M. Solid-state optical refrigeration to sub-100 kelvin regime. *Sci. Rep.* **6**, 20380 (2016).
103. Zhang, J., Li, D., Chen, R. & Xiong, Q. Laser cooling of a semiconductor by 40 Kelvin. *Nature* **493**, 504–508 (2013).
104. Zhang, S., Zhukovskyi, M., Jankó, B. & Kuno, M. Progress in laser cooling semiconductor nanocrystals and nanostructures. *NPG Asia Mater.* **11**, 54 (2019).
105. Fu, J. et al. Hot carrier cooling mechanisms in halide perovskites. *Nat. Commun.* **8**, 1300 (2017).
106. König, D. et al. Hot carrier solar cells: Principles, materials and design. *Phys. E: Low.-Dimens. Syst. Nanostruct.* **42**, 2862–2866 (2010).